

PVP2012-78122

SPECTRAL DIFFERENCE SOLUTION OF INCOMPRESSIBLE FLOW OVER AN INLINE TUBE BUNDLE WITH OSCILLATING CYLINDER

Christopher Cox*, Chunlei Liang†, Michael Plesniak‡

Department of Mechanical and Aerospace Engineering
The George Washington University
Washington, DC 20052

ABSTRACT

*A high-order spectral difference (SD) method for solving the Navier-Stokes equations on moving, deformable unstructured grids has been developed [1]. In this paper, the SD method and the artificial compressibility method (ACM) are integrated with a dual time-stepping scheme to model unsteady incompressible viscous flow past an inline tube bundle of cylinders equally sized (diameter = d) and spaced (spacing = $2.1 * d$) over an unstructured grid. Flow simulation results are obtained using a fourth-order space accurate SD method. Two forced oscillation cases are considered; (1) 1st cylinder oscillation and (2) 2nd cylinder oscillation. The Reynolds number used for both cases is 100 and the flow is laminar. Forced oscillation is performed in the transverse direction, and the subsequent altering of the flow physics of the system is studied. The frequency of vortex shedding behind each cylinder is the same. Root mean square results show that the lift coefficient is greatest for the 5th inline cylinder in both cases. Furthermore, a reduction in both lift and drag coefficients is seen from case (1) to case (2).*

INTRODUCTION

The fluid dynamics across an array of multiple cylinders is rich indeed. Studies carried out for two cylinders [2] identify nine flow patterns that are dependent upon angle of incidence and tube spacing. Induced separation of flow, shear layer reattachment and vortex synchronization are just a few of the phenomena that have been observed.

While flow around one or two cylinders has been greatly studied, fewer efforts have been devoted to studying a system involving many cylinders, commonly known as tube bundles. Tube bundles are widely used in power generation and oil industries (e.g. heat exchangers in nuclear reactors). Various tube bundle geometries exist; staggered symmetric, rotated square, normal triangle, parallel triangle, inline, etc. The focus of this paper is on the results of a study of two-dimensional incompressible flow past an inline tube bundle using the spectral difference method.

Steady and unsteady incompressible flow about an inline stationary tube bundle has previously been studied [3]. In this paper, however, unsteady incompressible flow across six inline cylinders with one cylinder exhibiting transverse oscillations will be studied within the context of the SD-ACM solver, which possesses the ability to move and deform the numerical grid such that the flow solution is properly computed as one of the cylinders oscillates.

*PhD Student, ccox@gwu.edu.

†Assistant Professor, corresponding author, chliang@gwu.edu

‡Professor, Department Chair, plesniak@gwu.edu

The following section describes the mathematical and numerical formulation of the aforementioned method, succeeded by sections involving validation studies, problem identification, results and conclusions.

MATHEMATICAL FORMULATION

Artificial Compressibility Method

The Navier-Stokes equations with artificial compressibility can be written in conservation form as

$$\frac{\partial Q}{\partial t} + \nabla F_I(Q) - \nabla F_V(Q, \nabla Q) = 0 \quad (1)$$

where the vector of conservative variables Q is

$$Q = \begin{bmatrix} p \\ u \\ v \end{bmatrix} \quad (2)$$

and the inviscid flux vector $F_I(Q)$ and viscous flux vector $F_V(Q, \nabla Q)$ are decomposed, respectively, into

$$F_I(Q) = f_I(Q) + g_I(Q) \quad (3)$$

where

$$f_I(Q) = \begin{bmatrix} \gamma u \\ u^2 + p \\ uv \end{bmatrix}, \quad g_I(Q) = \begin{bmatrix} \gamma v \\ uv \\ v^2 + p \end{bmatrix} \quad (4)$$

and

$$F_V(Q, \nabla Q) = f_V(Q, \nabla Q) + g_V(Q, \nabla Q) \quad (5)$$

where

$$f_V(Q, \nabla Q) = \begin{bmatrix} 0 \\ \nu u_x \\ \nu v_x \end{bmatrix}, \quad g_V(Q, \nabla Q) = \begin{bmatrix} 0 \\ \nu u_y \\ \nu v_y \end{bmatrix} \quad (6)$$

Here ρ is the density, ν is the kinematic viscosity, u and v are the velocity components in x and y directions, γ is a relaxation parameter, and $p = P/\rho$, where P represents the static pressure.

We define the element interface normal velocity as $V_n = un_x + vn_y$ and $c = \sqrt{V_n^2 + \gamma}$. The three characteristics for the above incompressible flow system with artificial compressibility are $V_n + c$, V_n and $V_n - c$.

The viscous fluxes can be computed using the following procedure:

1. Reconstruct Q_f at the flux points from the conservative variables at the solution points using Eqn. (18).
2. Average the field of Q_f on the element interfaces as $\overline{Q_f} = \frac{1}{2}(Q_f^L + Q_f^R)$. For interior flux points, $\overline{Q_f} = Q_f$. Meanwhile, appropriate boundary conditions shall be applied for specific edge flux points.
3. Evaluate ∇Q at solution points from $\overline{Q_f}$ using Eqns. (21,22) where $\nabla Q = \begin{bmatrix} Q_x \\ Q_y \end{bmatrix}$ and $Q_x = \frac{\partial Q}{\partial \xi} \xi_x + \frac{\partial Q}{\partial \eta} \eta_x$, etc.
4. Reconstruct ∇Q from solution points to flux points and using Eqn. (18), average them on the element interfaces as $\overline{\nabla Q_f} = \frac{1}{2}(\nabla Q_f^L + \nabla Q_f^R)$
5. Use $\overline{Q_f}$ and $\overline{\nabla Q_f}$ in order to compute the viscous flux vectors described in Eqn. (6) at the element interfaces.

Time Marching Scheme We write Eqn. (1) in a different form by adding a pseudo-time derivative term:

$$\frac{\partial Q}{\partial \tau_p} + R^*(Q) = 0 \quad (7)$$

where τ_p represents the pseudo time step and $R^*(Q) = \frac{\partial Q}{\partial t} + \nabla F_I(Q) - \nabla F_V(Q, \nabla Q)$.

Steady or unsteady flow solutions can be obtained with this solver. All computations utilize a fourth-order time accurate, strong stability-preserving five-stage Runge-Kutta scheme [4] for treating the pseudo time τ_p and a second-order backward Euler scheme to deal with the physical time marching; i.e. $\frac{\partial Q}{\partial t} \approx \frac{1}{2\Delta t} (3Q^* - 4Q^n + Q^{n-1})$.

Spectral Difference Method

The two-dimensional Navier-Stokes equations in Eqn. (1) can alternatively be written in conservation form

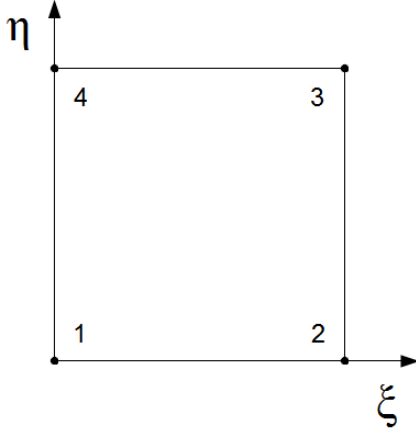


FIGURE 1. 2D COMPUTATIONAL ELEMENT. ($0 \leq \xi \leq 1$, $0 \leq \eta \leq 1$)

as

$$\frac{\partial Q}{\partial t} + \nabla \cdot \mathbf{F} = \frac{\partial Q}{\partial t} + \frac{\partial F}{\partial x} + \frac{\partial G}{\partial y} = 0 \quad (8)$$

where Q is the solution vector and F and G are the flux vectors, which contain both inviscid and viscous components.

The formulation of the SD method in this implementation follows from Liang et al. [5]. Considering the non-uniformity of the physical grid, one is motivated to transform the physical domain (x,y) into a computational domain (ξ,η) where the latter contains standard grid elements (see Fig. 1) over which the governing equations can be efficiently solved.

The transformation to the computational domain can be achieved using

$$\begin{bmatrix} x \\ y \end{bmatrix} = \sum_{i=1}^K M_i(\xi, \eta) \begin{bmatrix} x_i \\ y_i \end{bmatrix} \quad (9)$$

where K is the number of elemental nodes per element, (x_i, y_i) are the nodal cartesian coordinates, and $M_i(\xi, \eta)$ are the shape functions. As shown in Fig. 1, K is 4 in this implementation and node 1 is located at $(\xi, \eta) = (0,0)$. After the transformation into the computational domain, the governing equations for a *stationary* grid take on the following

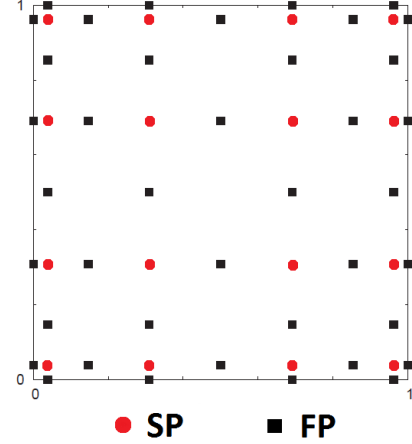


FIGURE 2. 2D DISTRIBUTION OF SOLUTION POINTS (SP) AND FLUX POINTS (FP) FOR A FOURTH-ORDER SPACE ACCURATE SD METHOD.

conservation form:

$$\frac{\partial \tilde{Q}}{\partial t} + \frac{\partial \tilde{F}}{\partial \xi} + \frac{\partial \tilde{G}}{\partial \eta} = 0 \quad (10)$$

where

$$\tilde{Q} = |J| \cdot Q \quad (11)$$

and

$$\begin{bmatrix} \tilde{F} \\ \tilde{G} \end{bmatrix} = |J| J^{-1} \begin{bmatrix} F \\ G \end{bmatrix} \quad (12)$$

The Jacobian J is computed for each standard element on the stationary grid using

$$J = \begin{bmatrix} x_\xi & x_\eta \\ y_\xi & y_\eta \end{bmatrix} \quad (13)$$

where the metrics of the Jacobian are obtained from the relationship between the non-uniform element and the standard element. The standard element contains two sets of points: solution points and flux points (see Fig. 2).

To construct a $(N - 1)$ degree polynomial in each coordinate direction, the solution at N points is required. Within

each dimension, the solution points are chosen as Gauss points defined by

$$X_s = \frac{1}{2} \left[1 - \cos \left(\frac{2s-1}{2N} \pi \right) \right], \quad s = 1, 2, \dots, N. \quad (14)$$

The flux points are chosen as Legendre-Gauss quadrature points plus the two end points 0 and 1, as suggested by Huynh [6]. Choosing $P_{-1}(\xi) = 0$ and $P_0(\xi) = 1$, the higher-degree Legendre polynomials can be determined by

$$P_n(\xi) = \frac{2n-1}{n} (2\xi-1)P_{n-1}(\xi) - \frac{n-1}{n} P_{n-2}(\xi) \quad (15)$$

The locations of these Legendre-Gauss quadrature points are the roots of the equation $P_n(\xi) = 0$. Using the solutions at N solution points, a $(N-1)$ degree polynomial can be built using the Lagrange basis

$$h_i(X) = \prod_{s=1, s \neq i}^N \left(\frac{X - X_s}{X_i - X_s} \right) \quad (16)$$

Similarly, using the fluxes at $(N+1)$ flux points, a N degree polynomial can be built using the Lagrange basis

$$l_{i+1/2}(X) = \prod_{s=0, s \neq i}^N \left(\frac{X - X_{s+1/2}}{X_{i+1/2} - X_{s+1/2}} \right) \quad (17)$$

The reconstructed solution vector in the 2D standard element is the tensor product of the two one-dimensional polynomials

$$Q(\xi, \eta) = \sum_{j=1}^N \sum_{i=1}^N \frac{\tilde{Q}_{i,j}}{|J_{i,j}|} h_i(\xi) \cdot h_j(\eta) \quad (18)$$

Similarly, the reconstructed flux vectors are obtained with

$$\tilde{F}(\xi, \eta) = \sum_{j=1}^N \sum_{i=0}^N \tilde{F}_{i+\frac{1}{2},j} \left[l_{i+\frac{1}{2}}(\xi) \cdot h_j(\eta) \right] \quad (19)$$

$$\tilde{G}(\xi, \eta) = \sum_{j=0}^N \sum_{i=1}^N \tilde{G}_{i,j+\frac{1}{2}} \left[h_i(\xi) \cdot l_{j+\frac{1}{2}}(\eta) \right] \quad (20)$$

The reconstructed fluxes are continuous across the entire element, but discontinuous across element interfaces. In this implementation, a simple Rusanov solver [7] is used to compute the inviscid fluxes across the interface. The derivatives of the inviscid fluxes are computed at the solution points using the derivatives of Lagrange operators l :

$$\frac{\partial \tilde{F}}{\partial \xi} \Big|_{i,j} = \sum_{r=0}^N \tilde{F}_{r+\frac{1}{2},j} \cdot l'_{r+\frac{1}{2}}(\xi_i) \quad (21)$$

$$\frac{\partial \tilde{G}}{\partial \eta} \Big|_{i,j} = \sum_{r=0}^N \tilde{G}_{i,r+\frac{1}{2}} \cdot l'_{r+\frac{1}{2}}(\eta_j) \quad (22)$$

To numerically handle the viscous effects at the element interfaces, an averaging approach [8, 9] is used.

Moving and Deforming Grid

To solve the Navier-Stokes equations on a moving and deforming domain, one can conveniently treat $x(\xi, \eta, \tau)$ and $y(\xi, \eta, \tau)$ as functions of the standard computational element consisting of dimensions in ξ , η and τ (see Fig. 3). In this case, τ coincides with the physical domain dimension t . The transformed components of $\nabla \cdot \mathbf{F}$ in Eqn. (8) then take on the form

$$\frac{\partial F}{\partial x} = \frac{\partial F}{\partial \xi} \cdot \xi_x + \frac{\partial F}{\partial \eta} \cdot \eta_x + \frac{\partial F}{\partial \tau} \cdot \tau_x \quad (23)$$

and

$$\frac{\partial G}{\partial y} = \frac{\partial G}{\partial \xi} \cdot \xi_y + \frac{\partial G}{\partial \eta} \cdot \eta_y + \frac{\partial G}{\partial \tau} \cdot \tau_y \quad (24)$$

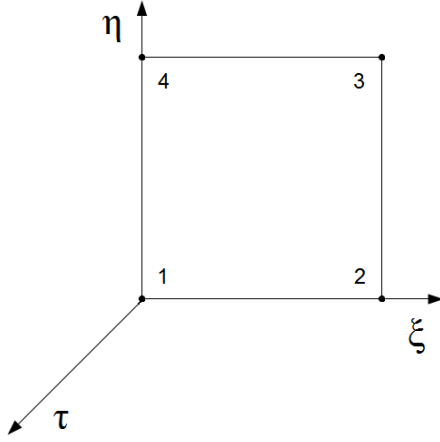


FIGURE 3. 2D COMPUTATIONAL ELEMENT FOR MOVING, DEFORMABLE GRID. ($0 \leq \xi \leq 1, 0 \leq \eta \leq 1, \tau \geq 0$)

The new Jacobian matrix is now expressed as

$$\mathcal{J} = \begin{bmatrix} x_\xi & x_\eta & x_\tau \\ y_\xi & y_\eta & y_\tau \\ 0 & 0 & 1 \end{bmatrix} \quad (25)$$

After some derivations, the Navier-Stokes equations are modified to take on the following conservation form in the computational domain

$$\frac{\partial \hat{Q}}{\partial \tau} + \frac{\partial \hat{F}}{\partial \xi} + \frac{\partial \hat{G}}{\partial \eta} = 0 \quad (26)$$

where

$$\begin{bmatrix} \hat{F} \\ \hat{G} \\ \hat{Q} \end{bmatrix} = |\mathcal{J}| \begin{bmatrix} \xi_x & \xi_y & \xi_\tau \\ \eta_x & \eta_y & \eta_\tau \\ 0 & 0 & 1 \end{bmatrix} \begin{bmatrix} F \\ G \\ Q \end{bmatrix} \quad (27)$$

To guarantee temporal stability and accuracy on moving, deformable domains, the discrete Geometric Conservation Law

$$\frac{\partial |\mathcal{J}|}{\partial \tau} + \frac{\partial (|\mathcal{J}| \xi_\tau)}{\partial \xi} + \frac{\partial (|\mathcal{J}| \eta_\tau)}{\partial \eta} = 0 \quad (28)$$

must be considered. After combining Eqns. 26 and 28, the following compact form is obtained and implemented within the numerical solver:

$$\frac{\partial Q}{\partial \tau} = \frac{1}{|\mathcal{J}|} \left\{ Q \left[\frac{\partial (|\mathcal{J}| \xi_\tau)}{\partial \xi} + \frac{\partial (|\mathcal{J}| \eta_\tau)}{\partial \eta} \right] - \left[\frac{\partial \hat{F}}{\partial \xi} + \frac{\partial \hat{G}}{\partial \eta} \right] \right\} \quad (29)$$

Combining Eqns. 7 and 29 provides a formulation to accomplish both physical and pseudo time marching.

The motion of the grid is prescribed by means of a blended-function technique which is similar to Persson et al. [10], Ou et al. [11] and Yu et al. [12].

Unstructured Mesh and Domain Decomposition

Figure 4 shows the unstructured mesh used in the flow simulation for the inline tube bundle. Multiple processors were utilized for the simulation and Fig. 5 shows the corresponding domain decomposition.

VALIDATION STUDY

Plunging Airfoil

Computational results for unsteady incompressible flow past a plunging airfoil at $Re = 1850$ have been obtained using the incompressible spectral difference with artificial compressibility (ISD-ACM) solver. An instantaneous pressure field for a downward plunging airfoil is shown in Fig. 6.

Time averaged statistics such as mean and root mean squared (*rms*) values are computed for both lift and drag coefficients. Results are compared to those obtained by a compressible spectral difference solver (See Tabs. 1 and 2). As expected, the effect of compressibility at these flow conditions is noticeable at a small scale.

TABLE 1. PLUNGING AIRFOIL MEAN AND RMS COMPARISON OF DRAG COEFFICIENT FOR INCOMPRESSIBLE AND COMPRESSIBLE FLOW.

$\{C_d\}$	Incompressible	Compressible
mean	0.042	0.039
rms	0.056	0.054

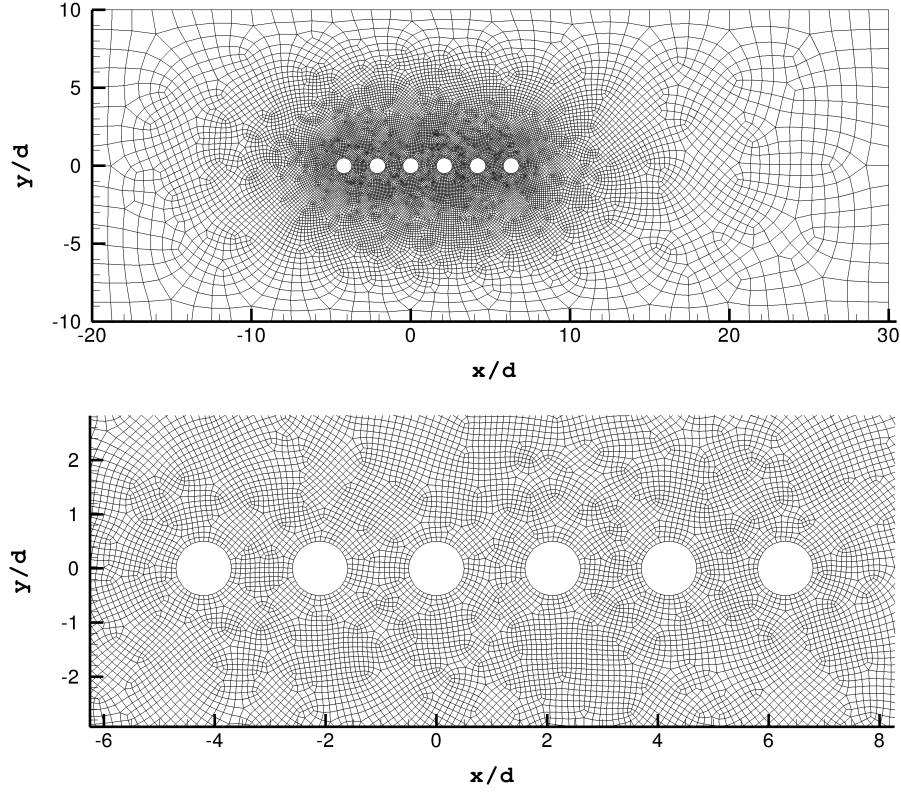


FIGURE 4. 2D UNSTRUCTURED INLINE TUBE BUNDLE PHYSICAL MESH.

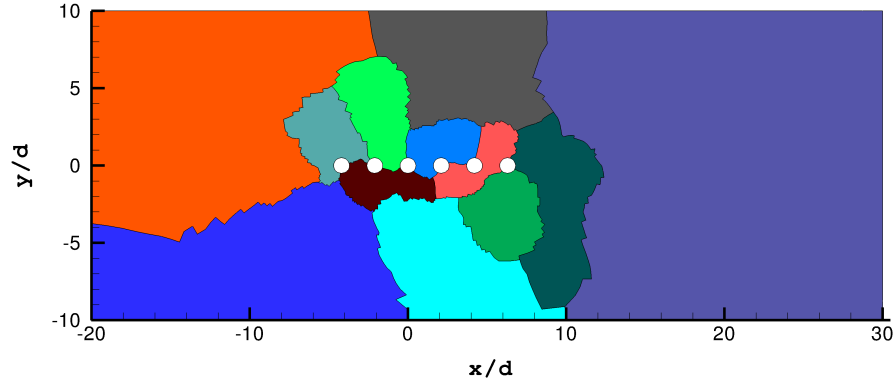


FIGURE 5. 2D UNSTRUCTURED INLINE TUBE BUNDLE SHOWING DOMAIN DECOMPOSITION.

Stationary Inline Tube Bundle

A stationary tube bundle has already been studied by Liang et. al [3], where results were obtained by a finite volume method over an unstructured grid for cylinder spacings ranging from $s = 2.1d$ to $s = 4.0d$, where d is the cylinder diameter. In this paper, the cylinder spacing is maintained at $s = 2.1d$. Streamline results obtained by the ISD-ACM

solver at $Re = 100$ are shown in Figure 7 for the stationary inline tube bundle. One can see the five recirculation zones, each one between the cylinders, and a weak vortex shedding behind the sixth cylinder. Mean and *rms* statistics for drag and lift are presented in Tabs. 3 and 4. Cylinder 2 exhibits a negative mean drag coefficient. The *rms* lift coefficient for cylinder 6 is the highest due to the slight

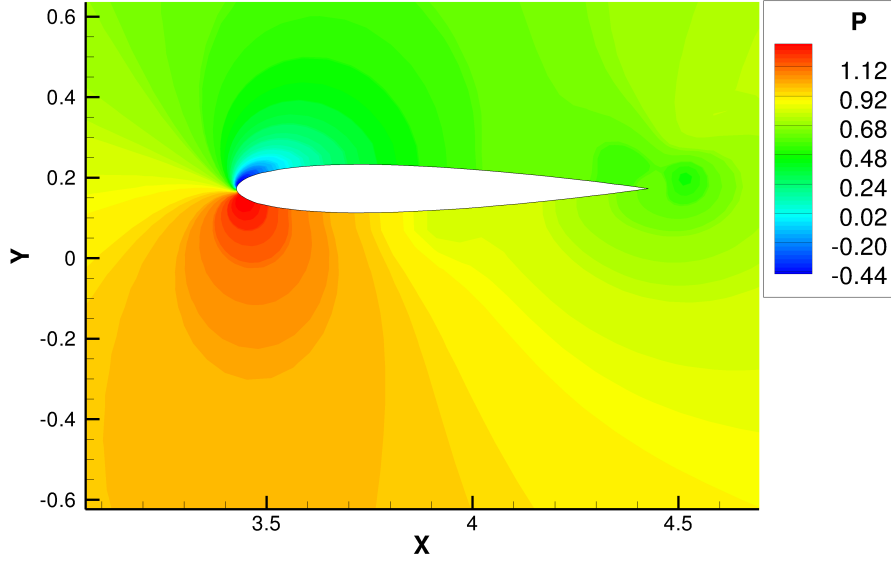


FIGURE 6. INSTANTANEOUS PRESSURE FIELD FOR A DOWNWARD PLUNGING AIRFOIL AT $Re = 1850$ PREDICTED BY A 4th ORDER ISD-ACM METHOD.

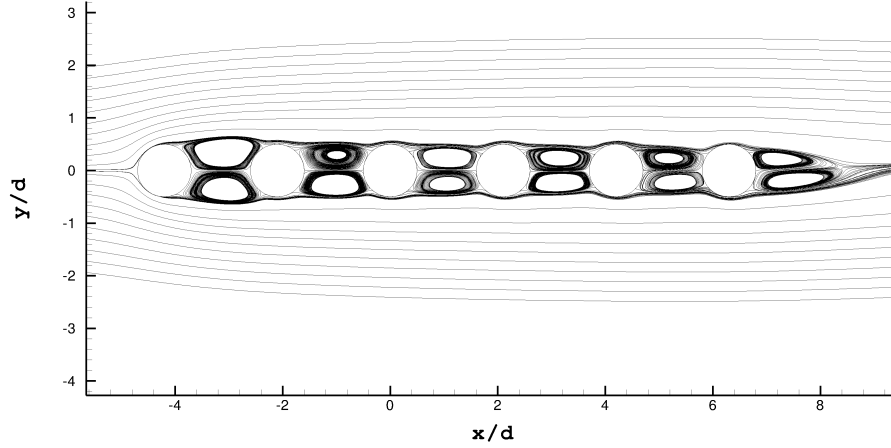


FIGURE 7. INSTANTANEOUS STREAMLINES PAST A STATIONARY INLINE TUBE BUNDLE AT $Re = 100$ PREDICTED BY A 4th ORDER ISD-ACM METHOD. CYLINDER SPACING EQUAL TO $2.1d$.

TABLE 2. PLUNGING AIRFOIL RMS COMPARISON OF LIFT COEFFICIENT FOR INCOMPRESSIBLE AND COMPRESSIBLE FLOW.

$\{C_l\}$	Incompressible	Compressible
rms	1.169	1.195

shedding of vortices behind the bundle.

INLINE TUBE BUNDLE WITH OSCILLATING CYLINDER

Liang et. al. [3] showed that as s increases the symmetry of the recirculation zones between the cylinders breaks, subsequently causing vortex shedding. Here, as stated previously, the cylinder spacing is maintained at the symmetry value of $s = 2.1d$; however, the break in symmetry in this paper results from the forced oscillation of cylinders. Thus,

TABLE 3. STATIONARY INLINE TUBE BUNDLE MEAN AND RMS DRAG COEFFICIENTS FOR CYLINDERS 1-6.

$\{C_d\}$	1	2	3	4	5	6
mean	1.078	-0.125	0.061	0.095	0.110	0.135
rms	1.078	0.125	0.061	0.095	0.110	0.135

TABLE 4. STATIONARY INLINE TUBE BUNDLE RMS LIFT COEFFICIENTS FOR CYLINDERS 1-6.

$\{C_l\}$	1	2	3
rms	1.21E-4	3.68E-4	5.37E-4
$\{C_l\}$	4	5	6
rms	9.23E-4	2.00E-3	3.00E-3

it is of interest to study the affect of cylinder oscillations on the vortex generation in the inline tube bundle system.

The 1st and 2nd inline cylinders are forced to oscillate in the transverse direction in the form of $Y(t) = A_e \cos(2\pi f_e t)$, where $A_e = 0.10d$ is the maximum oscillation amplitude. The Strouhal number, S_t , is computed using

$$S_t = \frac{f_e d}{U_\infty} \quad (30)$$

where f_e is the oscillation frequency, d is the diameter and U_∞ is the freestream velocity. The Strouhal number for the tubes is 0.10. This corresponds to a stationary tube bundle with cylinder spacing $s = 2.8$ as reported in [3].

Cylinder 1 Oscillations - Case(1)

Case(1) involves subjecting only cylinder 1 to forced oscillation. Figure 8 shows streamline results for this case. The pressure distribution around each cylinder for one period oscillation is shown in Fig. 9. For this type of oscillation in the tube bundle system, we obtain the time-averaged results for drag and lift coefficients seen in Tabs. 5 and 6. The drag coefficient, C_d , is highest for cylinder 1, lowest for cylinder 2, and increases from cylinders 2 to 6. The lift

coefficient is lowest for cylinder 1, increases from cylinders 1 to 5 and then drops slightly for the last cylinder. Note also that cylinder 4 exhibits a higher C_l than cylinder 6. The variation of instantaneous lift coefficients for all

TABLE 5. CASE(1) MEAN AND RMS DRAG COEFFICIENTS FOR CYLINDERS 1-6 FOR CYLINDER 1 OSCILLATIONS.

$\{C_d\}$	1	2	3	4	5	6
mean	1.154	-0.049	0.206	0.281	0.329	0.471
rms	1.154	0.055	0.208	0.287	0.348	0.494

TABLE 6. CASE(1) RMS LIFT COEFFICIENTS FOR CYLINDERS 1-6 FOR CYLINDER 1 OSCILLATIONS.

$\{C_l\}$	1	2	3	4	5	6
rms	0.147	0.411	0.493	0.570	0.604	0.529

cylinders can be seen in Fig. 10. This variation indicates a strong phase difference in the vortex shedding. For example, cylinder pair 2:3 shows a nearly 180° phase difference.

Cylinder 2 Oscillations - Case(2)

Case(2) involves subjecting only cylinder 2 to forced oscillation. Figure 11 shows streamlines results for this case. Pressure distributions for one period oscillation are shown in Fig. 12. Furthermore, time-averaged results for drag and lift coefficients can be seen in Tabs. 7 and 8. Similar to Case(1) above, C_d is highest for cylinder 1, lowest for cylinder 2, and increases from cylinders 2 to 6. The lift coefficient is lowest for cylinder 1, increases from cylinders 1 to 5 and then drops slightly for the last cylinder. However, note for this case that cylinder 6 exhibits a higher C_l than cylinder 4.

For cylinder 2 oscillations, the variation of instantaneous lift coefficients for all cylinders can be seen in Fig. 13.

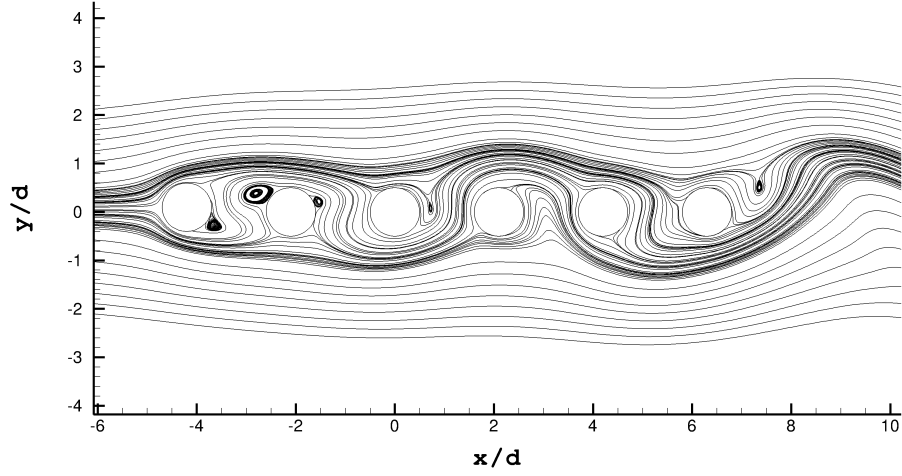


FIGURE 8. INSTANTANEOUS STREAMLINES FOR INLINE TUBE BUNDLE WITH THE 1st CYLINDER EXHIBITING TRANSVERSE OSCILLATIONS AT $Re = 100$. CYLINDER SPACING EQUAL TO $2.1d$.

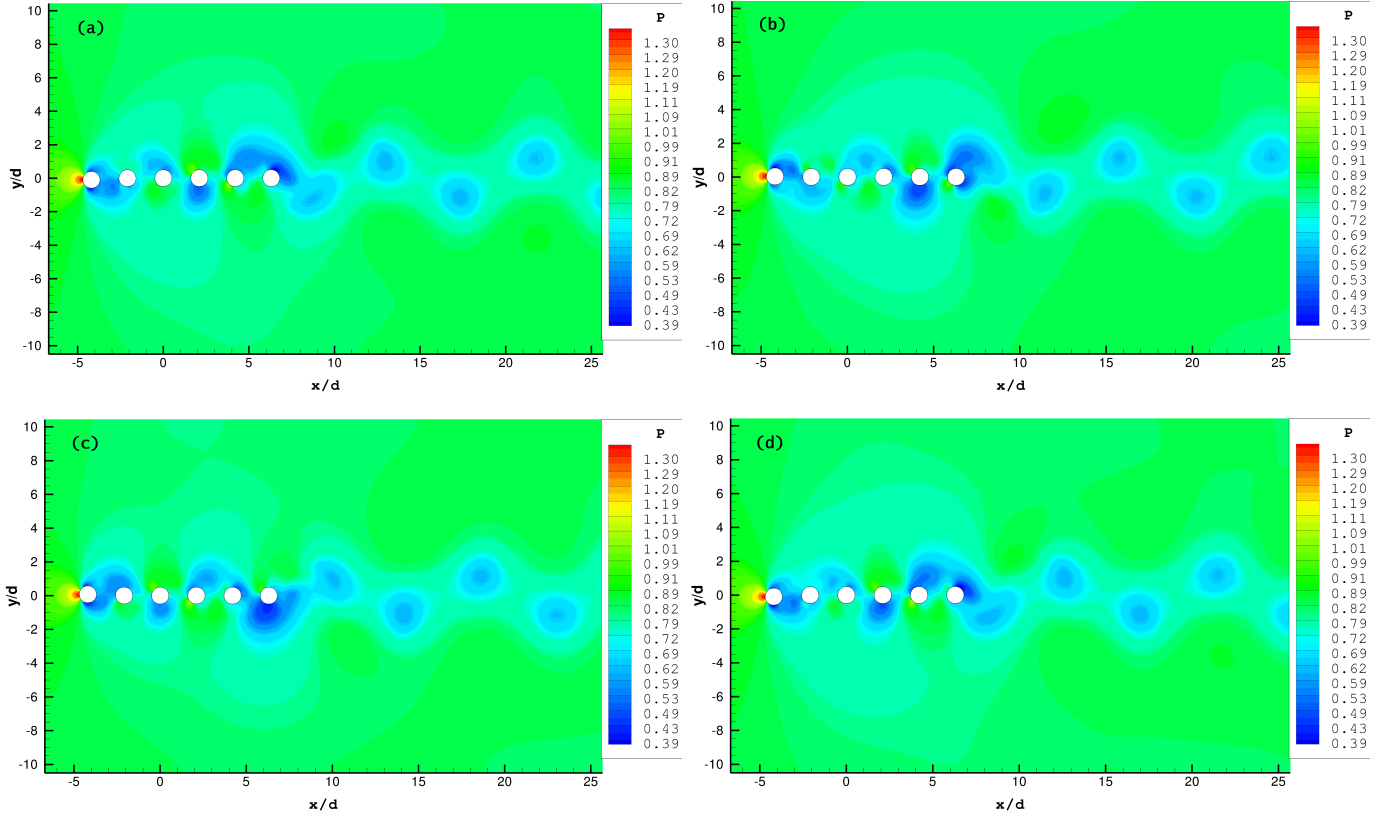


FIGURE 9. PRESSURE DISTRIBUTION FOR ONE OSCILLATION PERIOD (a)-(d) FOR INLINE TUBE BUNDLE WITH THE 1st CYLINDER EXHIBITING TRANSVERSE OSCILLATIONS AT $Re = 100$. CYLINDER SPACING EQUAL TO $2.1d$. PLOT (a) CORRESPONDS TO AN AMPLITUDE OF $-A_e$.

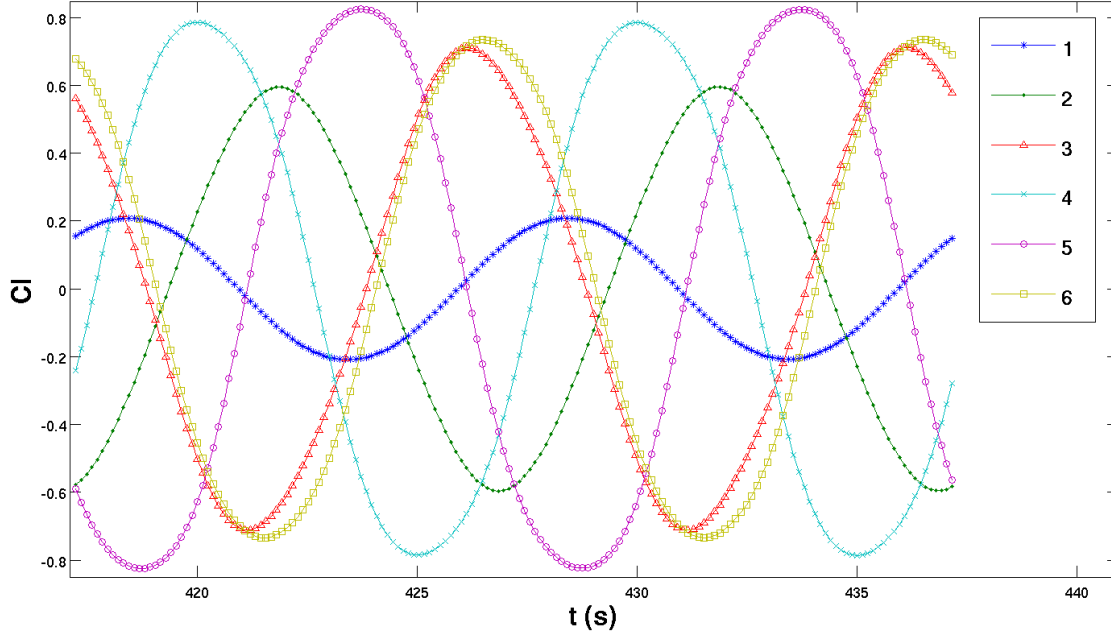


FIGURE 10. INSTANTANEOUS LIFT COEFFICIENT FOR ALL CYLINDERS 1-6 IN THE INLINE TUBE BUNDLE WITH THE 1st CYLINDER EXHIBITING TRANSVERSE OSCILLATIONS AT $Re = 100$. CYLINDER SPACING EQUAL TO $2.1d$.

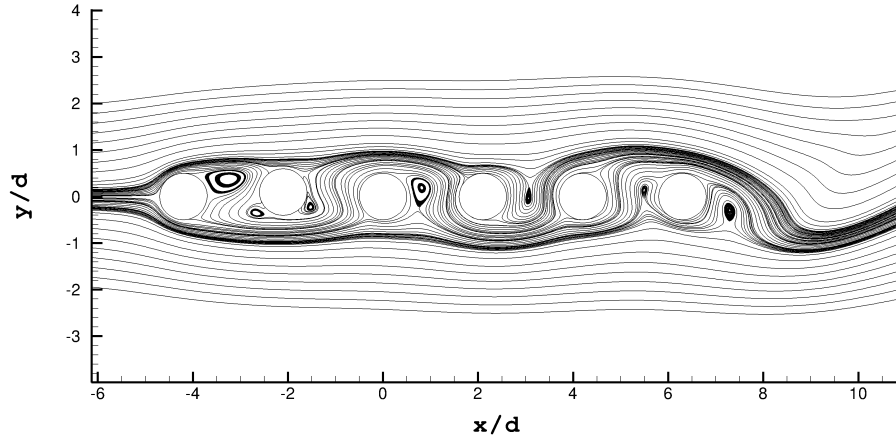


FIGURE 11. INSTANTANEOUS STREAM LINES FOR INLINE TUBE BUNDLE WITH THE 2nd CYLINDER EXHIBITING TRANSVERSE OSCILLATIONS AT $Re = 100$. CYLINDER SPACING EQUAL TO $2.1d$.

A strong phase difference in the vortex shedding is shown by the lift variation in cylinder pairs 2:3 and 3:4.

The results for both oscillation cases show that the *rms* C_l is greatest for the 4th inline cylinder and the *mean* C_d is negative for the 2nd inline cylinder. Also, a reduction in lift and drag is seen across the tube bundle when comparing *Case(2)* to *Case(1)*.

CONCLUSIONS

The spectral difference method with artificial compressibility and dual-time stepping is presented in this paper for an unstructured, moving, deformable grid. The solver is validated with numerical results obtained from a plunging airfoil and a stationary inline tube bundle. Unsteady incompressible flow simulations past an inline tube bundle with 1st and 2nd cylinder oscillations are presented. Both

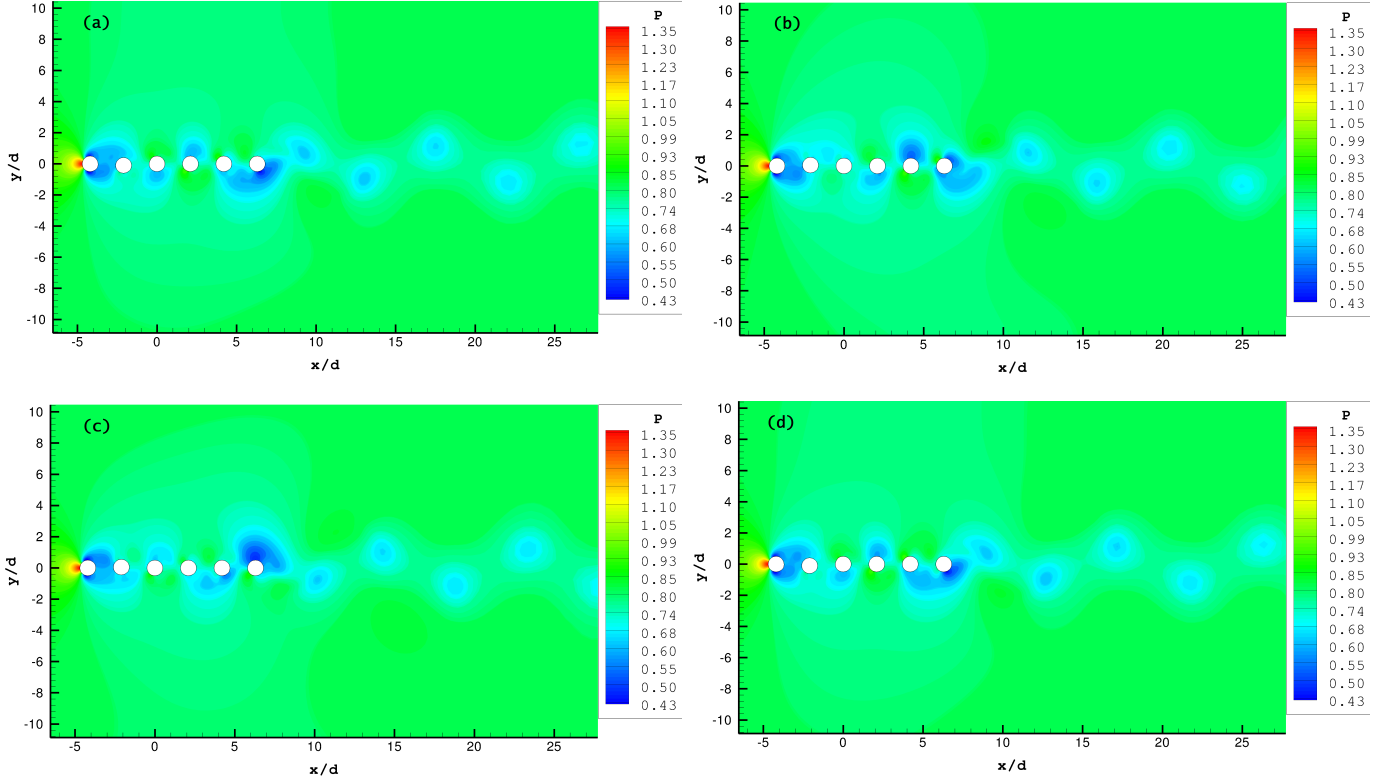


FIGURE 12. PRESSURE DISTRIBUTION FOR ONE OSCILLATION PERIOD (a)-(d) FOR INLINE TUBE BUNDLE WITH THE 2nd CYLINDER EXHIBITING TRANSVERSE OSCILLATIONS AT $Re = 100$. CYLINDER SPACING EQUAL TO $2.1d$. PLOT (a) CORRESPONDS TO AN AMPLITUDE OF $-A_e$.

TABLE 7. CASE(2) MEAN AND RMS DRAG COEFFICIENTS FOR CYLINDERS 1-6.

$\{C_d\}$	1	2	3	4	5	6
mean	1.122	-0.105	0.106	0.174	0.238	0.377
rms	1.122	0.105	0.107	0.175	0.242	0.387

TABLE 8. CASE(2) RMS LIFT COEFFICIENTS FOR CYLINDERS 1-6.

$\{C_l\}$	1	2	3	4	5	6
rms	0.057	0.109	0.299	0.354	0.430	0.402

types of oscillations break the streamline symmetry shown in Fig. 7 for cylinder spacing $s = 2.1d$. Mean and root mean square results of lift and drag coefficients are shown for each type of oscillation. The 2nd cylinder oscillation case reduces the lift coefficient for all cylinders when compared to the 1st cylinder oscillation case. Large variations in lift coefficients across the inline tube bundle have been obtained for both situations, indicating a strong phase difference in the vortex shedding of adjacent cylinders.

ACKNOWLEDGEMENTS

The first author would like to give many thanks to The George Washington University and the Department of Mechanical and Aerospace Engineering for financial support under the GW Presidential Merit Fellowship.

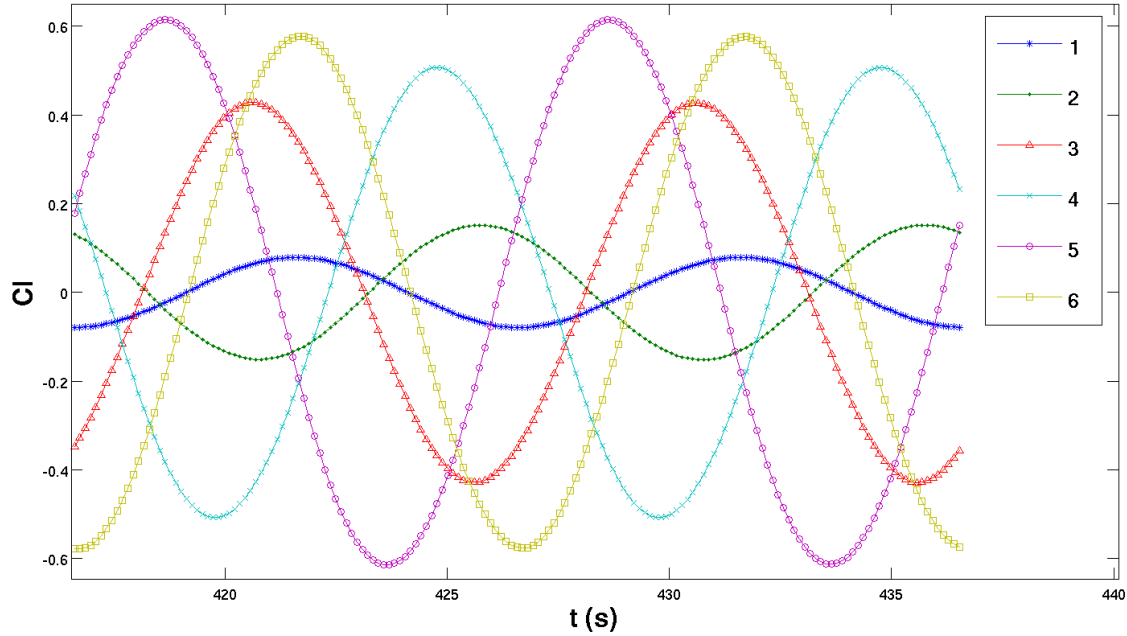


FIGURE 13. INSTANTANEOUS LIFT COEFFICIENT FOR ALL CYLINDERS 1-6 IN THE INLINE TUBE BUNDLE WITH THE 2nd CYLINDER EXHIBITING TRANSVERSE OSCILLATIONS AT $Re = 100$. CYLINDER SPACING EQUAL TO $2.1d$.

REFERENCES

- [1] Liang, C., Ou, K., Premasathan, S., Jameson, A., and Wang, Z., 2011. “High-order accurate simulations of unsteady flow past plunging and pitching airfoils”. *Computers and Fluids*, **40**(1), pp. 236–248.
- [2] Sumner, D., Price, S., and Paidoussis, M., 2000. “Flow-pattern identification for two staggered circular cylinders in cross-flow”. *Journal of Fluid Mechanics*, **411**, pp. 263–303.
- [3] Liang, C., Papadakis, G., and Luo, X., 2009. “Effect of tube spacing on the vortex shedding characteristics of laminar flow past an inline tube array: A numerical study”. *Computers and Fluids*, **38**, pp. 950–964.
- [4] Spiteri, R., and Ruuth, S., 2002. “A new class of optimal high-order strong-stability-preserving time discretization methods”. *SIAM Journal of Numerical Analysis*, **40**, pp. 469–491.
- [5] Liang, C., Chan, A., and Jameson, A., 2011. “A p-multigrid spectral difference method for incompressible navier-stokes equations.”. *Computers and Fluids*, **Vol. 51**, pp. 127–135.
- [6] Huynh, H., AIAA-2007-4079, 2007. “A flux reconstruction approach to high-order schemes including discontinuous galerkin methods”. *AIAA Paper*.
- [7] Rusanov, V., 1961. “Calculation of interaction of non-steady shock waves with obstacles”. *Journal of Computational and Mathematical Physics USSR*, **1**, pp. 267–279.
- [8] Sun, Y., Wang, Z., and Liu, Y., 2007. “High-order multidomain spectral difference method for the navier-stokes equations on unstructured hexahedral grids”. *Communication in Computational Physics*, **2**, pp. 310–333.
- [9] Kopriva, D., 1998. “A staggered-grid multidomain spectral method for the compressible navier-stokes equations”. *Journal of Computational Physics*, **143**, pp. 125–158.
- [10] Persson, P., Peraire, J., and Bonet, J., AIAA-2007-513, 2007. “Discontinuous galerkin solution of the navier-stokes equations on deformable domains”. *AIAA Paper*.
- [11] Ou, K., Liang, C., and Jameson, A., AIAA-2010-0541, 2010. “High-order spectral difference method for the navier-stokes equations on unstructured moving deformable grids”. *AIAA Paper*.
- [12] Yu, M., Wang, Z., and Hu, H., 2011. “A high-order spectral difference method for unstructured dynamic grids”. *Computers and Fluids*, **48**, pp. 84–97.